POLITECNICO DI TORINO
Repository ISTITUZIONALE

Disorder-Induced Degradation of Vertical Carrier Transport in Strain-Balanced Antimony-Based Superlattices

Original
Disorder-Induced Degradation of Vertical Carrier Transport in Strain-Balanced Antimony-Based Superlattices / Bellotti, E.; Bertazzi, F.; Tibaldi, A.; Schuster, J.; Bajaj, J.; Reed, M.. - In: PHYSICAL REVIEW APPLIED. - ISSN 2331-7019. - STAMPA. - 16:5(2021). [10.1103/PhysRevApplied.16.054028]

Availability:
This version is available at: 11583/2939345 since: 2021-11-22T13:56:40Z

Publisher:
APS

Published
DOI:10.1103/PhysRevApplied.16.054028

Terms of use:
openAccess

This article is made available under terms and conditions as specified in the corresponding bibliographic description in the repository

Publisher copyright

(Article begins on next page)

08 November 2022

Disorder-Induced Degradation of Vertical Carrier Transport in Strain-Balanced Antimony-Based Superlattices

E. Bellotti,[1,*] F. Bertazzi,[2] A. Tibaldi,[2] J. Schuster,[1,3] J. Bajaj,[3] and M. Reed[3]

[1] *Department of Electrical and Computer Engineering (ECE), Boston University, 8 Saint Mary's Street, Boston, Massachusetts 02215, USA*

[2] *Department of Electronics and Telecommunications (DET), Politecnico di Torino and IEIIT-CNR, Torino 10129, Italy*

[3] *U.S. Army Combat Capabilities Development Command (DEVCOM), Army Research Laboratory (ARL), 2800 Powder Mill Road, Adelphi, Maryland 20783-1138, USA*

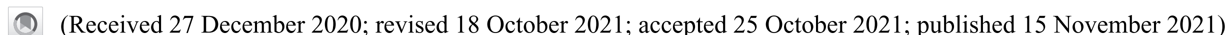

(Received 27 December 2020; revised 18 October 2021; accepted 25 October 2021; published 15 November 2021)

We investigate carrier transport in gallium-free strained-balanced $InAs/In_xAs_{1-x}Sb$ type-II superlattices in the presence of positional and compositional disorder. We use a rigorous nonequilibrium Green's function model based on fully nonlocal scattering self-energies computed in the self-consistent Born approximation and a multiband description of the electronic structure. Layer-thickness fluctuations, nonuniform antimony composition, and segregation throughout the superlattice stack lead to as-grown disordered structures that are quite different from the abrupt interface ideal superlattices. We find that regardless of its nature and cause, disorder significantly affects vertical-carrier-transport properties, by impeding the coherent propagation of carriers in the minibands. In particular, the minority-carrier hole mobility is fundamentally limited by the nonideal properties of the superlattice, namely the layer-thickness fluctuation and the nonuniform antimony distribution. Furthermore, upon reducing the temperature, holes become fully localized and transport occurs by hopping, which explains published measured detector data that demonstrates the quantum efficiency, exhibiting a very strong temperature dependence that degrades as the temperature is reduced. As a result, photodetectors that employ holes as minority carriers will be limited in performance, especially for long-wavelength infrared applications at low temperature. However, we find that minority-carrier electron mobility is largely unaffected by disorder, indicating the p-type absorbing layer as the preferred option.

DOI: 10.1103/PhysRevApplied.16.054028

I. INTRODUCTION

Infrared (IR) photodetectors (PDs) based on III–V semiconductor superlattices (SLs) are emerging as an alternative to more established technologies [1,2]. The potential advantages of III–V SLs stem from their relative technological maturity and larger industrial base when compared to II–VI compounds. Theoretical predictions of suppressed Auger recombination [3], together with experimentally measured lifetimes [4,5] in antimony-based type-II SLs (T2SLs), hold the promise for improved detector performance with respect to conventional bulk-type detectors. Specifically, gallium-free strain-balanced $InAs/In_xAs_{1-x}Sb$ T2SLs seem the most promising choice for imaging systems in the midwave infrared (MWIR) and long-wave infrared (LWIR) spectral ranges [6], due to the relatively longer carrier lifetimes [4,5]. While in the MWIR spectral region, imaging devices based on $InAs/In_xAs_{1-x}Sb$ T2SLs have delivered performance comparable to that of conventional indium antimonide cameras, a number of problems still remain for the LWIR spectral band. In particular, the low-temperature operation necessary to reduce dark current results in a degraded quantum efficiency (QE) due to incomplete carrier collection. Conversely, higher operating temperatures, where the QE is higher, lead to excessive dark current that degrades the image quality. QE degradation at low temperature is likely the result of a combination of degraded mobility and/or recombination processes due to the short carrier lifetime.

Recent experimental investigations [7,8] of vertical carrier transport in strain-balanced $InAs/In_xAs_{1-x}Sb$ T2SLs have shown that the hole mobility decreases with decreasing temperature, which is indicative of holes hopping through localized states rather than propagating coherently within the miniband [9]. Moreover, the large mobility anisotropy in the directions parallel and perpendicular to the growth axis leads to a degradation of the modulation transfer function (MTF) of the imaging array [10], resulting in compromised image quality and resolution.

*bellotti@bu.edu

 © 2021 American Physical Society

Figure 1 presents the typical structure of the absorber layer employed in a T2SL-based PD. In an ideal superlattice absorber, typically very close to the flat-band condition in barrier detectors, photogenerated carriers propagate coherently within minibands toward the corresponding contacts. The subband dispersion along the growth direction is crucially different for electrons and holes, the lowest conduction subband showing strong dispersion and the highest valence subband being almost dispersionless. This difference, rendered graphically by the different miniband widths for electrons and holes, has important consequences for carrier transport. In a nonideal SL, narrow minibands may be disrupted by energy misalignments and transport may occur by hopping and/or tunneling between different weakly coupled states.

The goal of this work is to investigate the physical mechanisms that are responsible for the less-than-optimal performance of LWIR-T2SLs based on $InAs/In_xAs_{1-x}Sb$ and determine if these limitations are technological, possibly related to the design or fabrication, or fundamental, inherent to the nature of the semiconductor material system used and consequently unsurmountable. Specifically, we intend to study how the temperature-dependent carrier mobility changes as a function of the SL structural parameters. Our approach, based on the nonequilibrium Green's function (NEGF) formalism, allows us to avoid making any *a priori* assumptions on the physical mechanisms that dominate the transport process.

Clearly, carrier mobility is only one aspect of the problem, since diffusion lengths also depend on carrier lifetimes. $InAs/In_xAs_{1-x}Sb$ T2SL lifetimes seem to be limited by Shockley-Reed-Hall (SRH) recombination [11] rather than intrinsic mechanisms [3]. In particular, carrier localization may favor spatially indirect SRH transitions [12], which calls for an atomistic description of the electronic structure. However, atomistic NEGF calculations are usually performed in the ballistic (coherent) limit and are restricted to a small number of atoms. Therefore, we focus our investigation on a mobility analysis and we infer device performance based on the measured values of the SRH lifetimes.

The paper is organized as follows. Section II describes the transport model and the approach used to introduce the disorder in the SL. Section III presents the calculated temperature-dependent mobility and compares it to the available experimental data. Section IV discusses the impact on device performance and Sec. V summarizes the findings.

II. A QUANTUM TRANSPORT MODEL

The NEGF formalism provides a fully quantum-mechanical treatment of carrier transport, describing phenomena such as carrier tunneling and hopping, without the uncontrolled approximations typically introduced by semiclassical approaches. Since as-grown T2SLs may be quite different from the intended structures designed with supposedly sharp heterointerfaces, we leverage available experimental information on the alloy and layer-by-layer composition of $InAs/In_xAs_{1-x}Sb$ SLs to guide the development of the model. The quantum-mechanical transport model employed in this study is presented in Refs. [9,13] and, for the sake of brevity, only the salient elements are repeated here. The complex subband structure of T2SLs is described using a $k \cdot p$ Hamiltonian that includes the first conduction band and heavy-hole, light-hole, and spin-orbit

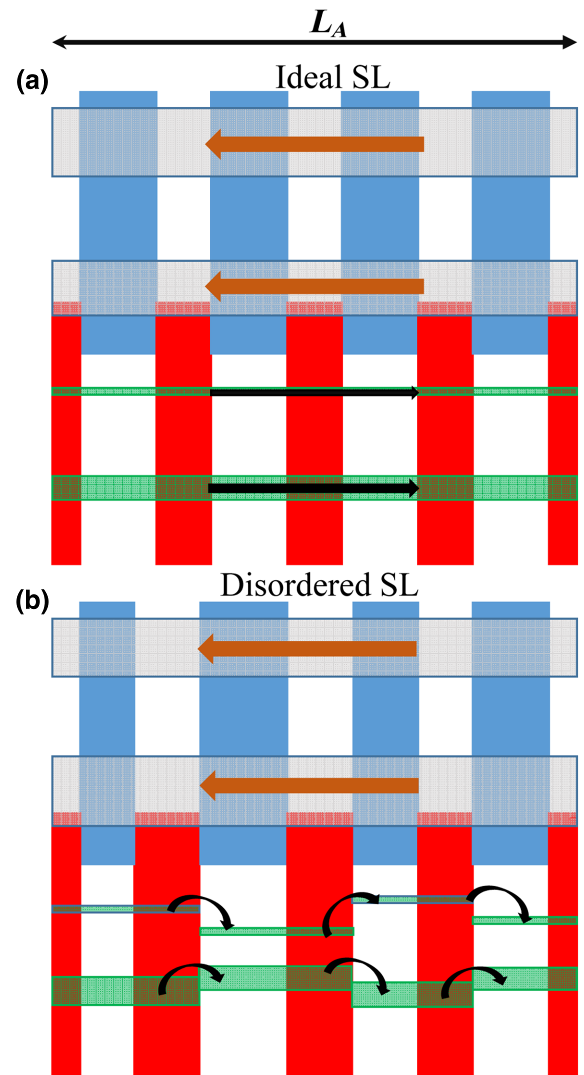

FIG. 1. The typical structure of the absorber layer employed in a T2SL-based PD close to the flat-band condition. Electrons and holes propagating toward the corresponding contacts in the minibands of a type-II SL (electrons to the left, holes to the right). (a) In a perfect SL, low-field carrier transport occurs in minibands (gray regions for electrons and green regions for holes). (b) In a nonideal SL, narrow minibands may be disrupted by energy misalignments and transport may occur by hopping between different weakly coupled states.

split-off bands [9]. For computational reasons, we limit our study to carrier transport along the z growth direction. For translationally invariant layered structures, the steady-state Dyson and Keldysh equations are [14–16]

$$G^R(z,z',E) = G_0^R(z,z',E) + \int dz_1 \int dz_2 G_0^R(z,z_1,E)\Sigma^R(z_1,z_2,E)G^A(z_2,z',E), \quad (1)$$

$$G^{\lessgtr}(z,z',E) = \int dz_1 \times \int dz_2 G^R(z,z_1,E)\Sigma^{\lessgtr}(z_1,z_2,E)G^A(z_2,z',E). \quad (2)$$

The retarded Green's function G^R provides the excitation spectrum of the SL and is related to the local density of states (LDOS). The lesser and greater Green's functions $G^{\lessgtr}$ describe how the states are occupied and determine the relevant one-particle properties, such as the charge and current densities. The total self-energy $\Sigma = \Sigma^B + \Sigma^{ep}$ includes the boundary self-energy Σ_B reflecting the openness of the system, which is obtained from the complex band structure of the reservoirs [15,17] and Σ_{ep}, which describes the interaction of carriers with acoustic and polar optical phonons within the deformation potential and the Fröhlich formalism, respectively. The direct numerical solution of the Dyson and Keldysh equations in a finite-element basis poses significant computational challenges due to the size of the structures we investigate. Therefore, the problem is formulated in a reduced-order mode-space representation, derived from the eigenstates of the noninteracting Hamiltonian. In order to reduce the number of basis functions while still satisfying conservation rules and accuracy, we partition the eigenstates of the nanostructure in two sets, a *near* set including the states with energy eigenvalues close to the range of interest, and a *remote* set including all the other eigenstates. Current conservation is recovered by formulating the problem using the near modes as basis functions and folding the influence of the remote modes in an additional self-energy [9].

While the concept of mobility is admittedly not germane to the NEGF formalism, the success of drift-diffusion approaches in predicting the performance of bulk $Hg_xCd_{1-x}Te$ detectors suggests that mobility calculations may be important to assess the potential of T2SL detectors. Different techniques have been proposed [18] to extract the mobility from quantum transport simulations. In the context of type-II SLs, electron and hole mobilities are computed, assuming transport to be drift dominated, from $v_{n,p} = \mu_{n,p}F$, where F is the electric field and $v_{n,p}$ are the electron and hole velocities:

$$v_{n,p} = \left\langle \frac{J_{n,p}}{\mp e\rho_{n,p}} \right\rangle, \quad (3)$$

where $\langle\cdot\rangle$ indicates a spatial average and the charge and current densities $\rho_{n,p}, J_{n,p}$ are obtained from [15,16]:

$$\rho_{n,p}(z) = \mp\frac{i}{\mathcal{A}}\sum_{\underline{k}}\int\frac{dE}{2\pi}G^{\lessgtr}(\underline{k},z,z,E), \quad (4)$$

$$J_{n,p}(z) = \lim_{z'\to z}\frac{e\hbar}{m_0}(\partial_z - \partial_{z'})\frac{1}{\mathcal{A}}\sum_{\underline{k}}\int\frac{dE}{2\pi}G^{\lessgtr}(\underline{k},z,z',E), \quad (5)$$

where e is the elementary charge, $\hbar$ is the reduced Planck's constant, and $\mathcal{A}$ is the normalization area.

A. A model for a disordered SL

We consider a T2SL with a unit cell composed of the sequence $In_{0.97}As_{1-0.03}Sb/In_{0.55}As_{1-0.45}Sb$, with thicknesses 10.2 nm and 2.1 nm, respectively (see the inset of Fig. 2). We assume that the SL is grown on a GaSb substrate that sets the lattice constant of the entire structure. As a result, the $In_{0.97}As_{1-0.03}Sb/In_{0.55}As_{1-0.45}Sb$ layers are under tensile and compressive strain, respectively. The subband structure of the T2SL, computed from the multiband 8×8 $k \cdot p$ model with Bloch boundary conditions, is reported in Fig. 2. The nominal cutoff wavelength is found to be $\simeq 10.8$ μm. Rather than plotting the energy dispersion in the growth direction in a separate panel, we employ vertical lines anchored to the corresponding energy values of the perpendicular wave number k_z, which allows to directly estimate the miniband widths as a function of the transverse wave number k_t (the subband dispersion is isotropic in the transverse plane). It should be immediately

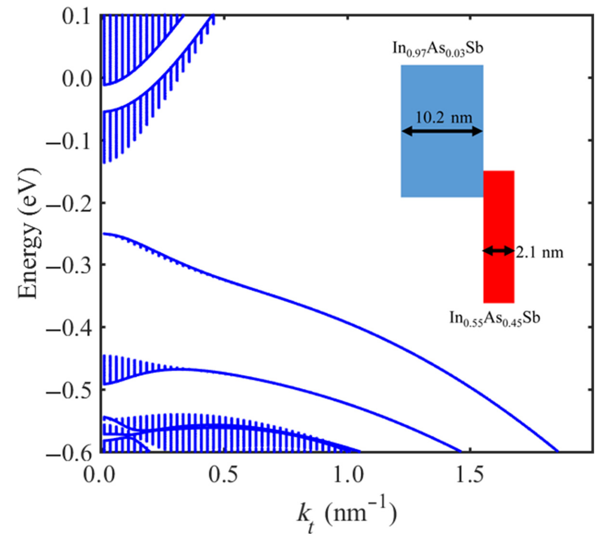

FIG. 2. The calculated energy bands as a function of the in-plane (solid lines) and perpendicular (vertical lines) wave vector, of an ideal $In_{0.97}As_{1-0.03}Sb/In_{0.55}As_{1-0.45}Sb$ SL with thicknesses of 10.2 nm and 2.1 nm, respectively.

noted that the top heavy-hole miniband is very narrow, with a width of approximately 4 meV at the center of the mini-Brillouin zone and increasing to 8 meV near the intermediate wave vector $k_t = 0.25$ nm^{-1}, where dispersion arises to band mixing. From this point forward, this structure is referred to as the ideal SL.

The inclusion of disorder breaks the periodicity of the SL in the growth direction. Consequently, one needs to consider a structure composed of N_u unit cells, long enough so that, when a suitable applied field F is applied, the Ohmic transport regime is reached. This condition can be checked by applying several electric field values and verifying that the carrier drift velocity increases linearly with the electric field.

Having defined an ideal finite-size SL, a model for the disorder has to be devised. The first approach is to consider variations in the thicknesses of the layers. We refer to this model as *positional* disorder. We assume that the molar fraction in each layer is uniform but that their thicknesses change layer by layer. Thickness variations can be introduced in the barriers, wells, or both. In practice, we include a variation of one monolayer (ML) in one or more randomly chosen layers, by shifting the layer boundary by one mesh element. This means that, if N_Δ is the number of perturbed layers, the average positional disorder for the finite SL is $N_\Delta/(2N_u)$ in ML units. For example, if $N_\Delta = 2N_u$, the average positional disorder is 1.0 ML, which is what we would normally expect for a realistic as-grown SL.

While the positional-disorder model provides a preliminary assessment of the impact of the layer variation on carrier transport, it does not describe the complex structural properties of InAs/$\text{In}_x\text{As}_{1-x}$Sb SLs [19–21]. Wood and coworkers [19] have found that antimony incorporation is delayed and there is significant migration out of the barrier region (with a higher expected Sb composition) to the well region (with a lower expected Sb composition). As a result, the change in antimony composition is not abrupt but varies smoothly over the SL period. Figure 3 presents a comparison between the expected ideal antimony composition (red line) and the measured value (black symbols). Based on this information, we can construct a *compositional*-disorder model for the disordered SL that mimics the behavior of the real SL. We start from an analytical expression that represents the measured antimony profile. We refer to this as the *migration envelope* and it is shown in Fig. 4 (blue line) along with the ideal profile (red line). Based on the migration envelope, we define a monolayer-by-monolayer antimony composition. The local antimony composition in each monolayer is included in the numerical model by assigning a value of the antimony molar fraction to each node of the finite-element mesh representing the SL. Subsequently, we generate a large number of unit cells with constant period d, in which the composition of each monolayer, shown by the blue bars in Fig. 4, is perturbed by a random amount; for

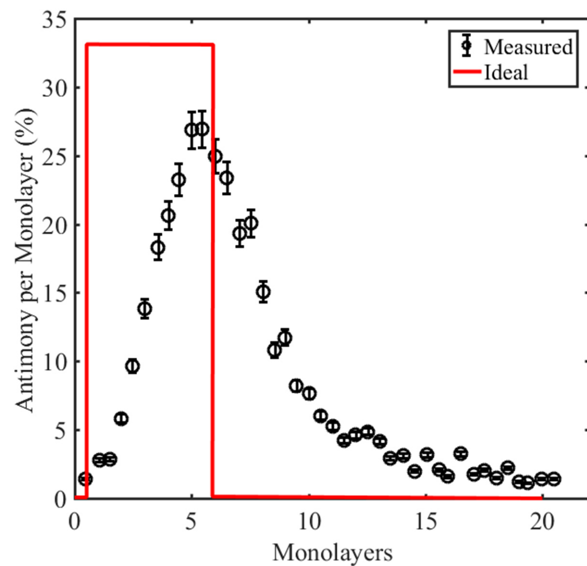

FIG. 3. The ideal (solid red line) and measured (black symbols) spatial antimony composition. The red line represents the ideal antimony molar fraction, while the black circles with vertical bars represent the measured antimony concentration as a function of the distance in monolayers in the unit cell. Data from Ref. [19].

example, 10% of the antimony concentration maximum value. Each of these random cells, characterized by a unique compositional-disorder configuration, presents the same average antimony distribution.

Starting from a set of random unit cells with compositional disorder, we can compute the energy gaps of an equal number of different SLs, each of which is generated by the periodic repetition of a unique cell. The distribution of cutoff wavelengths is presented in Fig. 5(a). It can be seen that, as a consequence of the lower confinement caused by the smooth antimony distribution, the cutoff shifts toward shorter wavelengths. This information can potentially be used to assess the level of compositional disorder of the SL. If one wants to compensate for the loss of confinement without changing the size of the cell, then the amount of antimony in the barrier needs to be increased. For example, increasing the molar fraction of the barrier layer from 45% to 50% while keeping the same migration envelope, the average cutoff wavelength moves back closer to the nominal value, as shown in Fig. 5(b). To create a finite-size SL with compositional disorder, we pick N_u random unit cells and stitch them together.

III. RESULTS AND DISCUSSION

We address first the case of electron transport considering ideal and disordered SLs. Since the simulation domain is terminated with open boundary conditions (i.e., semi-infinite contact regions on both sides), we set the initial and

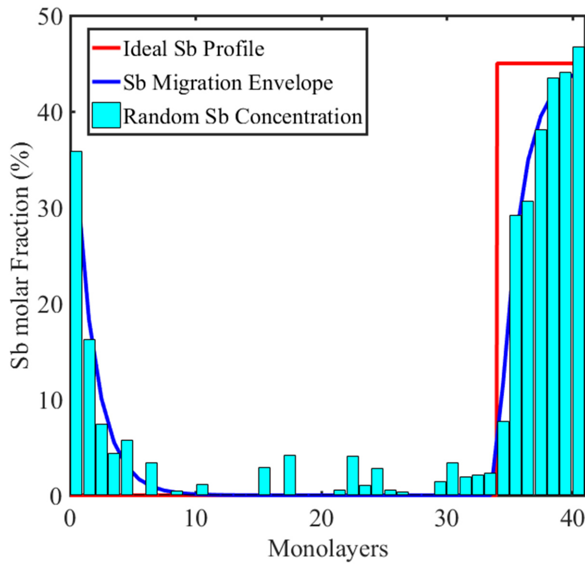

FIG. 4. The antimony concentration profile for a SL unit cell with antimony migration. The red line represents the ideal antimony concentration profile. The blue line is the expected antimony migration envelope based on experimental measurements and the light blue bars are the monolayer-by-monolayer antimony concentration with a random variation on the nominal value within each unit cell.

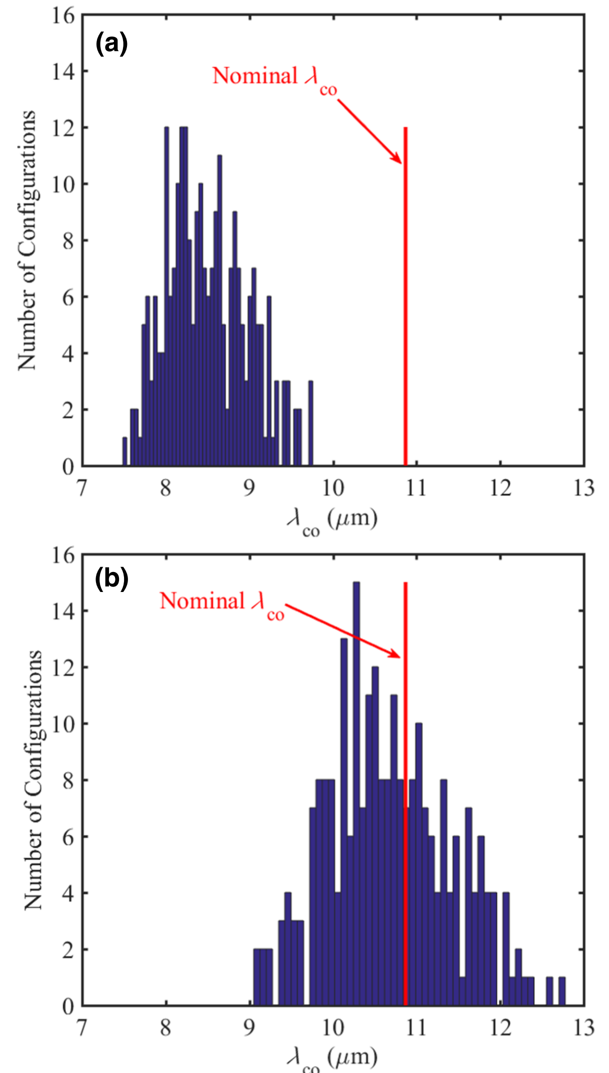

FIG. 5. The distribution of cutoff wavelengths for 250 different SL unit cells with compositional disorder: the distribution with a maximum antimony concentration of (a) 45% and (b) 50%. In both (a) and (b), the red line labeled $\lambda_{co} = 1.24/E_g$ is the cutoff wavelength for the ideal SL with the electronic structure presented in Fig. 2.

final layers of the SL to be InAs, so that there are no barriers that can impede electron injection or extraction. While this may not always be true in a realistic device, it allows us to better understand the intrinsic nature of the SL transport processes. We compute the electron drift velocity using Eq. (3) and derive the vertical mobility for the ideal SL as a function of the temperature [9,13]. We apply an electric field strength of 300 V/cm; in the case of electrons, this value is not critical, since the conduction miniband is wide. Furthermore, for each temperature, we compute the Fermi energy at equilibrium, so that an electron concentration of $n_o = 1.0 \times 10^{15}$ cm^{-3} is present in the SL. For the disordered SLs, we keep the same values of the Fermi energies and verify *a posteriori* that the average electron concentration is the same as the one for the ideal SL. Convergence at each temperature is reached when the total current is constant in the entire device.

Figure 6 presents the calculated mobility for the ideal SL (blue line with open circles) as described in Sec. II A. We can immediately note that the mobility decreases monotonically, from 20 000 cm^2 V^{-1} s^{-1} at 30 K down to 9000 cm^2 V^{-1} s^{-1} at 200 K, as the temperature increases. While this behavior is typical of transport limited by phonon scattering, the temperature dependence is not $T^{-3/2}$, as expected in a bulk semiconductor [22], but it approaches $T^{-3/4}$ at high temperatures and $T^{-1/4}$ at low temperatures. This weak temperature dependence suggests that electron transport in the ideal SL is predominately coherent at low temperature, as one can deduce from the analysis of the spectral current. The phonon contribution is only marginal at the highest temperatures, when interactions with phonons increase. As a result, for the ideal SL, coherent processes dominate transport in the conduction miniband.

However, when disorder is included, the nature of the transport changes. The electron mobility computed for the SL with a 1.0-ML positional disorder is presented in Fig. 6, with a dashed-dotted orange line with open squares. Overall, the mobility is lower by a factor of approximately 2 and the temperature dependence changes. At lower temperatures, the mobility first increases slightly and then

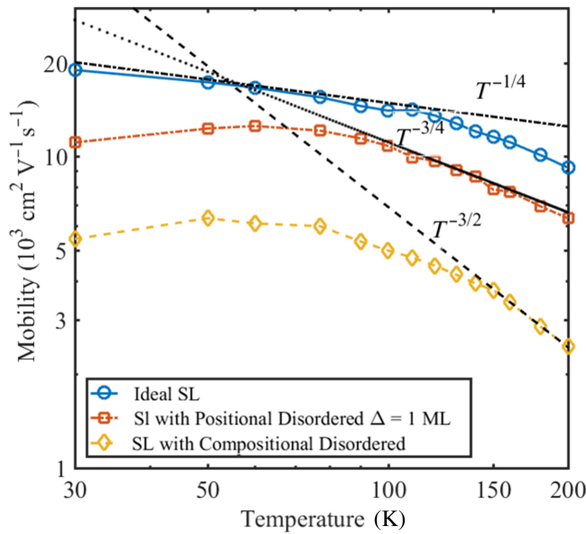

FIG. 6. The calculated electron mobility (blue line with circles) for an ideal SL and a nominal cutoff wavelength of $\simeq$ 10.8 μm. When a positional disorder of 1 ML is introduced, the electron mobility decreases (dashed-dotted red line with squares). A further decrease is observed (yellow line with diamonds) when compositional disorder is included. The dotted, dashed-dotted, and dashed black lines provide a guide for the eye to identify different temperature dependencies.

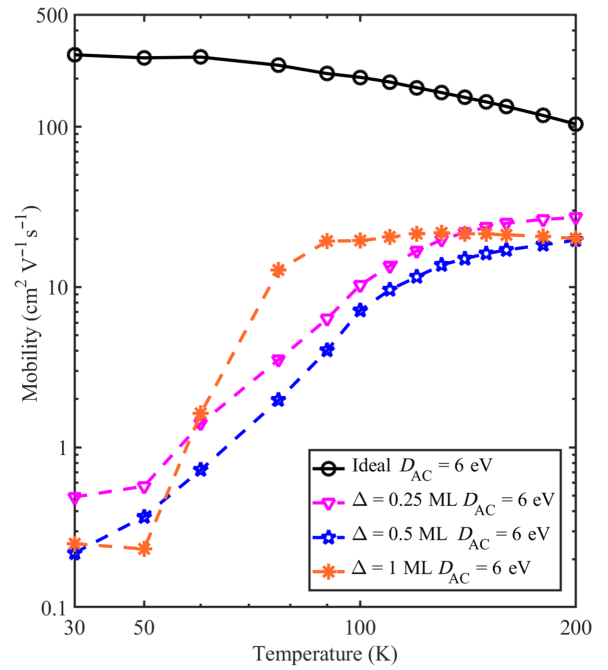

FIG. 7. The calculated hole mobility as a function of the temperature for a LWIR SL and with different values of *positional disorder*. The solid black line with circles represents the calculated mobility for the ideal SL. The calculated values for a SL with a positional disorder of 0.25 ML are reported as the purple line with downward-pointing triangles. The dashed blue line with pentagrams and the orange line with asterisks are the calculated values for positional disorder of 0.5 ML and 1 ML, respectively.

decreases again as the temperature increases. This behavior can be traced back to the fact that at low temperatures, most electrons are located at the bottom of the conduction miniband. As a result, depending on the amount of disorder-induced misalignment of the energy states, hopping between bottom states may take place even if the overall miniband width is large. As temperature increases, the mobility decreases, again approaching a temperature dependence of $T^{-3/4}$. Note that a 1.0-ML positional disorder introduces a modest perturbation in the conduction miniband and this is probably the best outcome for a realistic SL that can be obtained during growth. Finally, when we consider the case of the SL with compositional disorder, we obtain the mobility represented by the yellow line with open diamond reported in Fig. 6. Qualitatively, the temperature dependence is similar to that of the previous case of positional disorder, with two quantitative differences. First, the overall mobility is approximately four times lower and, at high temperatures, the $T^{-3/2}$ temperature dependence is observed. We now turn our attention to hole transport. The mobility values calculated for the ideal SL described in Sec. II A are reported in Fig. 7 (black line with open circles). As expected (due to the large hole effective mass), the mobility is significantly lower than that for electrons even in the ideal SL. Due to the narrow miniband, the transport is coherent only if the applied electric field is small. When phonon interactions contribute to the majority of the spectral current, in the high-temperature limit, we observe a $T^{-3/2}$ dependence.

Figure 7 presents the calculated hole mobility for three SLs with increasing level of positional disorder, 0.25 ML (dashed purple line with downward-pointing triangles), 0.5 ML (dashed blue line with pentagrams), and 1 ML (dashed orange line with asterisks). A striking feature can immediately be noted, i.e., the dramatic decrease in mobility values, up to 2 orders of magnitude at low temperatures. These results are in both qualitative and quantitative agreement with what has been measured by Olson [7] for LWIR SLs and more recently by Casias [8] for MWIR SLs. It is important to emphasize that, as the disorder increases, the misalignment of the energy level in the SL destroys the coherent miniband transport further, reducing the mobility at the lowest temperatures. Moreover, in the low-temperature region, holes tend to become localized and movement can only occur through hopping processes. For the case of a disorder of 1 ML, which is the best outcome for an as-grown SL, the hole mobility is drastically suppressed when compared to the ideal case. A final observation is that positional disorder is clearly responsible for both the reduction of mobility and the *inversion* of the temperature dependence.

To gain additional insight into the nature of hole transport in a disordered SL, we consider the case of *compositional disorder*. Figure 8 presents the calculated temperature-dependent hole mobility for a SL obtained from the ideal one, by including compositional disorder as explained in Sec. II A. Furthermore, to verify how phonon scattering impacts the mobility, one can change the strength of the acoustic phonon interaction by reducing or increasing the deformation potential parameter. As a result, we compute the hole mobility for three different values of the acoustic deformation potential, $D_{\rm AC} = 1$ eV, 6 eV, and 12 eV. Changing the acoustic deformation potential results in different amount of broadening of the LDOS, changing the energy separation between the localized states that result from the disorder breaking up the minibands. We can immediately note that, in the case of $D_{\rm AC} = 6$ eV, the calculated mobility (dashed purple line with upward-pointing triangles) is between 1 and 2 orders of magnitude lower than the ideal case (black line with open circles). Furthermore, the temperature dependence is significantly different than that of the ideal SL. The mobility rapidly increases with temperature and decreases slightly only at high temperatures. The reduction of $D_{\rm AC}$ to 1 eV (dashed blue line with pentagrams) leads to greatly suppressed hopping and tunneling probabilities due to the smaller energy states broadening, with the consequence that the mobility drops by an additional order of magnitude. Additionally, the mobility peak value is reached at a higher temperature than before and the subsequent drop is less pronounced. If we increase $D_{\rm AC}$ to 12 eV (dashed orange line with asterisks), we observe the opposite outcome, i.e., the mobility increases. Figure 9 presents the local density of state calculated at a temperature of 64 K and for $D_{\rm AC} = 6$ eV (the default value used for all simulations in this work). When the acoustic scattering rate is reduced, the energy states of the disordered SL are less broadened and have little overlap. When the scattering rate is increased, a significant energy-level broadening is present, augmenting the probability of hopping and tunneling. The intensity of the blue speckles represents the LDOS plotted using the same numerical scale. Based on this result, it is reasonable to state that in this kind of SL, as the temperature is decreased, holes become more and more localized and require an activation energy to hop and/or tunnel between states to be collected by the contacts.

In order to identify possible thermally activated processes and the associated activation energies, Fig. 10 shows the same data available in Fig. 8 but as a function of the inverse temperature. Additionally, we include the mobility values measured by Olson and coworkers [7] (yellow diamonds) and Donetsky and coworkers [23] (green downward-pointing triangles), both sets being obtained for LWIR SLs. The experimental data from Ref. [7] exhibit two distinct slopes with two different activation energies; the first, at low temperatures, with an

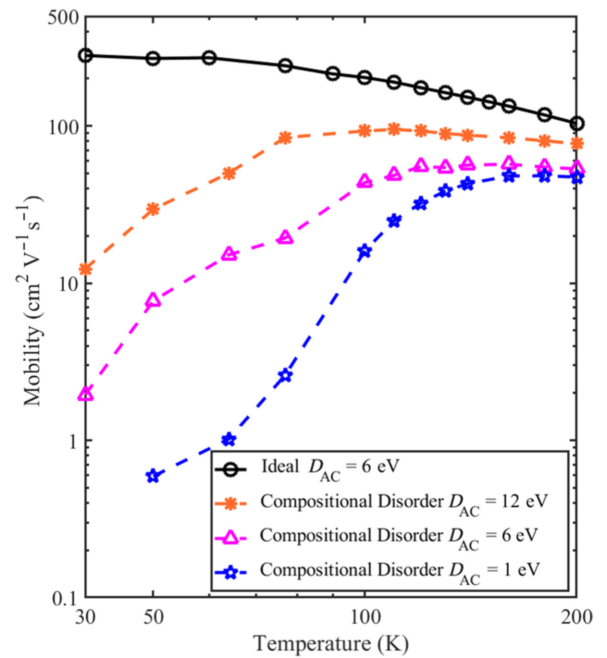

FIG. 8. The calculated hole mobility as a function of the temperature for three SLs with LWIR cutoff wavelengths and different values of the acoustic deformation potential. The solid black line with circles presents the values calculated for the ideal SL. The dashed orange line with asterisks, the purple line with upward-pointing triangles, and the light blue line with pentagons represent the calculated hole mobilities of the SL with compositional disorder, and for three different acoustic deformation potential values $D_{\rm AC} = 12$ eV, 6 eV, and 1 eV, respectively.

activation energy of $E_a^L = 16$ meV, and the second, at relatively higher temperatures, equal to $E_a^H = 36$ meV. The authors of Ref. [7] posit that at higher temperatures (greater than 110 K), hole transport occurs in extended Bloch states and, as the temperature decreases, hole transport is controlled by a trap with a mobility edge and an activation energy of 36 meV. Upon further reduction of the temperature, holes become fully localized and transport occurs by phonon-assisted hopping with an activation energy of 16 meV.

Considering the calculated mobility values for the SL with compositional disorder in the two cases of $D_{\rm AC} =$ 12 eV and 6 eV, a similar behavior can be identified. For temperatures below 77 K and $D_{\rm AC} = 12$ eV, the estimated activation energy is 13.4 meV. For temperatures below 100 K and $D_{\rm AC} = 6$ eV, the calculated activation energy increases to 16.7 meV. These values are very similar to the values that Olson and coworkers [7] found in the hopping region. Furthermore, the two sets of calculated values, for $D_{\rm AC} = 12$ eV and 6 eV, bracket the experimental data from Ref. [7].

It is possible to correlate these activation energies with the energy misalignments in the localized states of

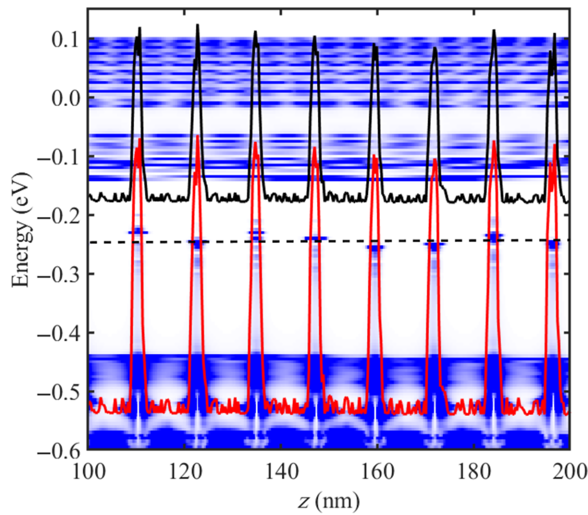

FIG. 9. The LDOS calculated for the LWIR SL examined in this work operating at 64 K, including compositional disorder. The calculated LDOS is obtained using an acoustic deformation potential value of $D_{\mathrm{AC}} = 6$ eV. The solid black and red lines represent the calculated conduction- and valence-band profiles of the SL, respectively. As a result of the antimony migration, the profiles of the bands change as the composition varies. The intensity of the blue speckles represent variations of the LDOS. It can be seen that the presence of scattering broadens the energy states, leading to a higher mobility, as shown in Fig. 8.

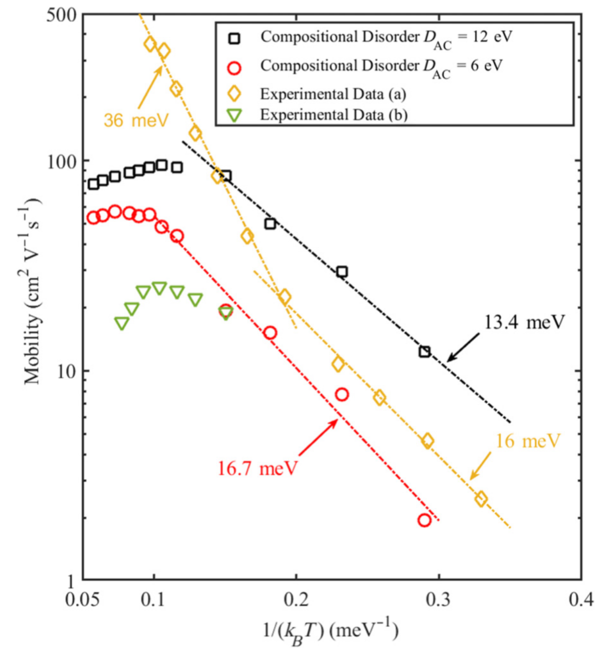

FIG. 10. A comparison between the measured and calculated hole mobility for LWIR SLs. The theoretical data are obtained for the SL including compositional disorder and two values of the acoustic deformation potential, $D_{\mathrm{AC}} = 12$ eV (black squares) and $D_{\mathrm{AC}} = 6$ eV (orange circles). The measured values included as a comparison are for a LWIR SL from Ref. [7] (yellow diamond) and another LWIR SL from Ref. [23] (green downward-pointing triangles).

the topmost valence miniband, located at approximately −0.25 eV in the ideal SL, identified with a dashed black line in Fig. 9. The standard deviations of the LDOS peaks (see, e.g., Fig. 9) with respect to the center of the unperturbed miniband are 10 meV, 15.5 meV, and 20 meV, for $D_{\mathrm{AC}} = 12$ eV, 6 eV, and 1 eV, respectively. The standard deviations can be interpreted as the energy needed for a trapped hole to move from one energy state to another one in a neighboring SL period. The standard-deviation values obtained for $D_{\mathrm{AC}} = 12$ eV and 6 eV (10 meV and 15.5 meV) are in reasonable agreement with the activation energies obtained from the theoretical mobility curves corresponding to the same deformation potentials. We conclude that for the T2SL analyzed in this work, at low temperature, antimony migration disrupts the miniband and introduces localized traplike states that lead to hopping transport.

For temperatures above 120 K, the calculated mobilities for all values of D_{AC} decrease slightly with increasing temperature, indicating a transition from hopping transport to miniband transport, resulting from the increased thermal energy. This transition can also be observed in the experimental data from Donetsky and coworkers [23]. Moreover, the calculated mobility values do not exhibit a clear transition from hopping to mobility edge transport. This could be due to the more complex nature of the disorder, including three-dimensional features, in the real T2SL that the present model does not capture.

Finally, we want to point out that Casias and coworkers [8] have found a similar dual-slope behavior for MWIR SL, with activation energies comparable to the values obtained in this work and by Olson [7]. Nevertheless, it is also interesting to note that the measured values presented by Casias [8] for a MWIR SL are comparable to what we compute for our LWIR prototype SL and the other experimental values. All these experimental and theoretical data suggest that for $\mathrm{InAs/In}_x\mathrm{As}_{1-x}\mathrm{Sb}$, type-II SL hole transport is limited by the current technological maturity of the material system, namely the disorder introduced by the antimony migration.

IV. IMPACT ON DETECTOR PERFORMANCE

Based on the discussion is Sec. III, in the case of electrons, positional and compositional disorder causes a reduction of mobility, with minor modification of its temperature dependence. One can evaluate the impact of these changes on detector performance by looking at the electron diffusion length and the internal QE. Even with a minimum electron mobility of 2000 cm^2 V^{-1} s^{-1} at 200 K (6000 cm^2 V^{-1} s^{-1} at 77 K) and assuming a quite low

minority-carrier lifetime of 35 ns [24], the diffusion length would be in excess of 11 μm at 200 K (12 μm at 77 K). To estimate the internal QE [see Ref. [25], p. 756, Eq. (29)], one needs to know the absorption coefficient and the thickness of the absorber layer L_A. Assuming a PD with LWIR cutoff wavelength, an absorption layer thickness of $L_A = 5\ \mu$m, and an average absorption coefficient of 500 cm^{-1} [10], the QE at 200 K would be 49% (51% at 77 K), with no reflection at the surface of the PD. This value is adequate for imaging applications that do not require high performance. Consequently, for the case of minority electrons, vertical mobility is not the limiting factor in detector performance. Rather, the short lifetime and the low absorption coefficients are the limiting factors.

When holes are minority carriers, the diffusion length is drastically reduced. In fact, even assuming a 412 ns [5] hole lifetime at 77 K (using the same value at 200 K) and a corresponding hole mobility of 25 cm^2 V^{-1} s^{-1} at 77 K, and 50 cm^2 V^{-1} s^{-1} at 200 K (for $D_{\rm AC} = 6$ eV), the hole diffusion lengths would be $L_p = 2.6\ \mu$m and $L_p = 5.9\ \mu$m, respectively. The corresponding QEs are 31% and 40%, with no reflection at the surface of the PD. As a result, for holes, the limiting factors are both the low absorption coefficients and the low mobility.

This initial evaluation indicates that significant material developments are needed to improve device performance. These efforts should be directed toward increasing the absorption coefficients, the electron minority-carrier lifetime, and the minority hole mobility. This is necessary in order to improve the quantum efficiency of these PDs to be able to compete with the established technologies.

V. CONCLUSION

We present a numerical study of the carrier transport properties in antimonide-based superlattices intended for infrared detector applications. We employ a rigorous one-dimensional quantum-mechanical transport model based on the NEGF formalism that includes a $k \cdot p$ description of the electronic structure. This approach allows us to avoid making any *a priori* assumptions on the physical mechanism (tunneling, sequential tunneling, or hopping) that dominates the transport. We compute the temperature-dependent electron and hole mobilities for the an ideal SL with a cutoff wavelength in the long-wave infrared region. Furthermore, we include two kinds of disorder, positional disorder, where the thickness of the layers is changed by up to one monolayer, and compositional disorder, where we introduce an antimony profile based on experimental data. We find that in the case of electrons, while the mobility is degraded by the disorder, we still observe an increasing mobility as the temperature is decreased. Nevertheless, even for severe disorder, the electron mobility is large enough so that carrier collection is not compromised even for modest carrier lifetimes and detector performance; namely, the QE can be adequate. For holes, we arrive at completely different outcomes. Hole transport at low temperature is dominated by hopping. As a result, hole mobility decreases as the temperature is lowered. An analysis of the activation energies shows that both the theoretical and experimental data indicate the presence of an activation energy that correlates with the experimentally observed energies and with the calculated trapping energy of the valence miniband resulting from the antimony migration.

This study indicates that, regardless of its nature and cause, disorder introduces severe limitations to the vertical hole transport properties of gallium free strain-balanced $InAs/In_xAs_{1-x}Sb$ type-II superlattices. We also carry out an initial estimation of the detector quantum efficiency for either minority electrons or holes. We find that for electrons, the mobility degradation, while present, is not as severe and the limiting factor to obtaining a high QE is the low value of the optical absorption coefficient. In the case of holes, both the low mobility and optical absorption coefficient values are responsible for the reduction in quantum efficiency. These limitations become particularly dramatic at the low operating temperatures that are normally required to reduce noise and dark current. Furthermore, when holes are the minority carriers that contribute to the device photocurrent, the degradation of their transport coefficient is so drastic that the operation of detector may not be as good as the current state-of-the-art technologies.

ACKNOWLEDGMENTS

We wish to thank R. E. DeWames for guiding us to the study of transport in superlattices and for his constant feedback and encouragement. We also wish to thank D. Rhiger, D. Ting, and S. Svensson for many discussions and C. Morath and G. Aryawansa for providing experimental mobility data. This work was supported by the U.S. Army Research Laboratory's Center for Semiconductor Modeling (CSM [26]) under Contract No. W911NF-18-2-0027, managed by Dr. M. Reed. The development of the computational tools was supported by the U.S. Army Research Laboratory through the Collaborative Research Alliance for Multi-Scale Multidisciplinary Modeling of Electronic Materials (Grant No. W911NF-12-2-0023). The computational resources were provided by the U.S. Department of Defense (DoD) High-Performance Computing (HPC) Systems and the 2019 Army Research Office Defense University Research Instrumentation Program (DURIP) Award (Grant No. W911NF-19-1-0161).

[1] P. Klipstein, E. Avnon, D. Azulai, Y. Benny, R. Fraenkel, A. Glozman, F. Hojman, O. Klin, L. Krasovitsky, L. Langof,

I. Lukomsky, M. Nitzani, I. Shtrichman, N. Rappaport, N. Snapi, E. Weiss, and A. Tuito, in *SPIE Defense+Security, Infrared Technology and Applications XLII*, Proceedings of the SPIE Vol. 9819 (SPIE - The international Society of Optics and Photonics, Baltimore, Maryland, 2016), p. 98190T.

[2] D. Ting, A. Soibel, A. Khoshakhlagh, L. Höglund, K. Sam, S. Rafol, C. Hill, A. Fisher, E. Luong, N. Jean, J. Liu, J. Mumolo, B. Pepper, and S. Gunapala, in *SPIE Defense+Security, Infrared Technology and Applications XLIII*, Proceedings of the SPIE Vol. 10177 (SPIE - The international Society of Optics and Photonics, Anaheim, California, 2017), p. 101770N.

[3] C. Grein, M. Flatté, J. Olesberg, S. Anson, L. Zhang, and T. Boggess, Auger recombination in narrow-gap semiconductor superlattices incorporating antimony, Appl. Phys. Lett. **92**, 7311 (2002).

[4] E. Steenbergen, B. Connelly, G. Metcalfe, H. Shen, M. Wraback, D. Lubyshev, J. M. Fastenau, A. Liu, S. Elhamri, O. Cellek, and Y.-H. Zhang, Significantly improved minority carrier lifetime observed in a long-wavelength infrared III–V type-II superlattice comprised of InAs/InAsSb, Appl. Phys. Lett. **99**, 251110 (2011).

[5] B. Connelly, E. Steenbergen, H. Smith, S. Elhamri, W. Mitchel, S. Mou, G. Metcalfe, G. Brown, and M. Wraback, Dependence of minority carrier lifetime of Be-doped InAs/InAsSb type-II infrared superlattices on temperature and doping density, Phys. Status Solidi B **253**, 630 (2016).

[6] D. Rhiger, E. Smith, B. Kolasa, J. Kim, J. Klem, and S. D. Hawkins, Analysis of III–V superlattice *n*B*n* device characteristics, J. Electron. Mater. **45**, 4646 (2016).

[7] B. V. Olson, J. F. Klem, E. A. Kadlec, J. K. Kim, M. D. Goldflam, S. D. Hawkins, A. Tauke-Pedretti, W. T. Coon, T. R. Fortune, E. A. Shaner, and M. E. Flatté, Vertical Hole Transport and Carrier Localization in $InAs/InAs_{1-x}Sb_x$ Type-II Superlattice Heterojunction Bipolar Transistors, Phys. Rev. Appl. **7**, 024016 (2017).

[8] L. Casias, C. Morath, E. Steenbergen, J. L. G.A. Umana-Membreno, P. T. Webster, J. Kim, G. Balakrishnan, L. Faraone, and S. Krishna, Vertical carrier transport in strain-balanced InAs/InAsSb type-II superlattice material, Appl. Phys. Lett. **166**, 182109 (2020).

[9] F. Bertazzi, A. Tibaldi, M. Goano, J. A. Gonzalez Montoya, and E. Bellotti, Non-Equilibrium Green's Function Modeling of Type-II Superlattice Detectors and Its Connection to Semiclassical Approaches, Phys. Rev. Appl. **14**, 014083 (2020).

[10] J. Schuster, Assessment of the modulation transfer function in infrared detectors with anisotropic material properties: Type-II superlattices, IEEE Trans. Electron Devices **66**, 1338 (2019).

[11] Y. Aytac, B. Olson, J. Kim, E. Shaner, S. Hawkins, J. Klem, M. Flatté, and T. F. Boggess, Temperature-dependent optical measurements of the dominant recombination mechanisms in InAs/InAsSb type-2 superlattices, J. Appl. Phys. **118**, 125701 (2015).

[12] Z.-Y. Lin, S. Liu, E. Steenbergen, and Y.-H. Zhangb, Influence of carrier localization on minority carrier lifetime in InAs/InAsSb type-II superlattices, Appl. Phys. Lett. **107**, 201107 (2015).

[13] A. Tibaldi, J. A. Gonzalez Montoya, M. G. C. Alasio, A. Gullino, A. Larsson, P. Debernardi, M. Goano, M. Vallone, G. Ghione, E. Bellotti, and F. Bertazzi, Analysis of Carrier Transport in Tunnel-Junction Vertical-Cavity Surface-Emitting Lasers by a Coupled Nonequilibrium Green's Function−Drift-Diffusion Approach, Phys. Rev. Appl. **14**, 024037 (2020).

[14] S. Steiger:, Ph.D. thesis, Eidgenössische Technische Hochschule Zürich, 2009.

[15] U. Aeberhard, Ph.D. thesis, Eidgenössische Technische Hochschule Zürich, 2008.

[16] F. Bertazzi, M. Goano, G. Ghione, A. Tibaldi, P. Debernardi, and E. Bellotti, in *Handbook of Optoelectronic Device Modeling and Simulation*, edited by J. Piprek (CRC Press, Boca Raton, Florida, 2017), chapter 2, p. 35.

[17] M. Luisier, A. Schenk, W. Fichtner, and G. Klimeck, Atomistic simulation of nanowires in the $sp^3d^5s^*$ tight-binding formalism: From boundary conditions to strain calculations, Phys. Rev. B **74**, 205323 (2006).

[18] Y.-M. Niquet, V.-H. Nguyen, F. Triozon, I. Duchemin, O. Nier, and D. Rideau, Quantum calculations of the carrier mobility: Methodology, Matthiessen's rule, and comparison with semiclassical approaches, J. Appl. Phys. **115**, 054512 (2014).

[19] M. Wood, K. Kanedy, F. Lopez, M. Weimer, J. Klem, S. Hawkins, E. Shaner, J.K. Kim, Monolayer-by-monolayer compositional analysis of InAs/InAsSb superlattices with cross-sectional STM, J. Cryst. Growth **425**, 110 (2015).

[20] J. Lu, E. Luna, T. Aoki, E. Steenbergen, Y. Zhang, and D. Smith, Evaluation of antimony segregation in $InAs/InAs_{1-x}Sb_x$ type-II superlattices grown by molecular beam epitaxy, J. Appl. Phys. **119**, 095702 (2016).

[21] N. Kotulak, J. Nolde, M. Katz, M. Twigg, K. Knipling, D. Lubyshev, J. Fastenau, A. Liu, and E. Aifer, Three-dimensional visualization of Sb segregation in InAs/InAsSb superlattices using atom probe tomography, J. Appl. Phys. **128**, 015302 (2020).

[22] G. Neudeck and R. Pierret, eds., *Fundamental of Carrier Transport*, Modular Series on Solid State Devices Vol. X (Addison-Wesley, New York, 1990).

[23] J. Liu, D. Donetski, K. Kucharczyk, G. Kepshidze, G. Belenky, and S. Svensson, Short-period InAsSb-based strained layer superlattices for high quantum efficiency long-wave infrared detectors (personal communication).

[24] B. Olson, E. Shaner, J. Kim, J. Klem, S. Hawkins, M. Flatte, and T. Boggess, Identification of dominant recombination mechanisms in narrow-bandgap InAs/InAsSb type-II superlattices and InAsSb alloys, Appl. Phys. Lett. **103**, 052106 (2013).

[25] S. Sze, *Physics of Semiconductor Devices* (John Wiley & Sons, New York, 1981).

[26] M. Reed, J. Bajaj, F. Bertazzi, E. Bellotti, J. Schuster, and P. Perconti, in *SPIE—Quantum Sensing and Nano Electronics and Photonics XV*, Proceedings of the SPIE Vol. 10540 (SPIE - The international Society of Optics and Photonics, San Francisco, California, 2018), p. 1054005.